Earth Planet. Sci. Lett. 624 (2023) 118438

Contents lists available at ScienceDirect

Earth and Planetary Science Letters

journal homepage: www.elsevier.com/locate/epsl

Mercury isotope constraints on the timing and pattern of magmatism during the end-Triassic mass extinction

Xia Hua [a], Runsheng Yin [b], David B. Kemp [a,*], Chunju Huang [a], Jun Shen [c], Xin Jin [d]

[a] State Key Laboratory of Biogeology and Environmental Geology and Hubei Key Laboratory of Critical Zone Evolution, School of Earth Sciences, China University of Geosciences, Wuhan 430074, China
[b] State Key Laboratory of Ore Deposit Geochemistry, Institute of Geochemistry, Chinese Academy of Sciences, Guiyang 550081, China
[c] State Key Laboratory of Geological Processes and Mineral Resources, China University of Geosciences, Wuhan 430074, China
[d] State Key Laboratory of Oil and Gas Reservoir Geology and Exploitation, Chengdu University of Technology, Chengdu 610059, China

ARTICLE INFO

Edited by: Prof A Jacobson

Keywords:
End-Triassic Mass Extinction (ETME)
Central Atlantic Magmatic Province (CAMP)
Mercury isotopes
Mercury cycle

ABSTRACT

The End-Triassic Mass Extinction (ETME) was broadly coincident with the emplacement of the Central Atlantic Magmatic Province (CAMP). However, the relationship between evolutionary phases of CAMP (i.e. prolonged shallow intrusive pulses and later extrusives) and the ETME is not clear. Here, a high-resolution record of changing magmatic activity is established using mercury (Hg) isotopes through a Triassic-Jurassic sedimentary succession deposited on the northern flank of CAMP. Successive negative and positive mass independent fractionation (MIF) of odd Hg isotopes through the end-Triassic interval in this succession suggest dominantly thermogenic Hg release from intrusive heating of organic-rich sedimentary rocks, followed by mainly volcanogenic input of mantle-sourced Hg. This inferred pattern is also supported by correlations to available CAMP ages. Minimum calculated volumes of thermogenic and volcanogenic Hg needed to drive the observed shifts at the basin-scale are plausible based on likely CAMP Hg release volumes, and biotic turnover in the studied region was unlikely to have occurred before the onset of volcanogenic Hg release.

1. Introduction

The End-Triassic Mass Extinction (ETME), one of the largest Phanerozoic mass extinctions, resulted in the extinction of marine invertebrate species and major megafloral turnovers on land (McElwain et al., 1999; van de Schootbrugge et al., 2009). The approximate temporal coincidence between the ETME and the emplacement of the Central Atlantic Magmatic Province (CAMP) suggests that voluminous carbon released during CAMP emplacement triggered a global environmental perturbation and biological crisis (Hesselbo et al., 2002; Mchone, 2003; Schoene et al., 2010; Blackburn et al., 2013; Wotzlaw et al., 2014; Davies et al., 2017; Heimdal et al., 2018; Ruhl et al., 2020; Capriolo et al., 2021; Lindström et al., 2021). CAMP emplacement involved prolonged intrusive activity, with extrusive activity indicated by rarely preserved basalts around the continental area of North America, South America, Africa and Europe (Davies et al., 2017; Marzoli et al., 2018, 2019). Available U-Pb zircon ages suggest that major shallow intrusive activity began earlier than basaltic lava pulses (Schoene et al., 2010; Blackburn et al., 2013; Davies et al., 2017; Heimdal et al., 2018; Lindström et al., 2021). CAMP volcanogenic gasses (CO_2, SO_2, halocarbons and phytotoxic pollutants including Hg and other heavy metals) have been considered major contributers to end-Triassic climate change and extinction (Marzoli et al., 2018; Lindström et al., 2019, 2021; Grasby et al., 2020). Recent studies have stressed thermogenic degassing from magma-sediment interaction in continental large igneous provinces could have been a potential driver of warming and extinction in the geological record (Burgess et al., 2017; Heimdal et al., 2018; Berndt et al., 2023; Svensen et al., 2023). However, the timing and amount of volatiles emitted during different CAMP stages are not well understood, and the relative timing/pace of different CAMP stages and their relationship to the global ETME remain unclear due to the limited temporal resolution of available records and the common geographic separation between records of CAMP volcanism and stratigraphic records of extinction. This hinders understanding of the environmental effects of magmatism, and in particular the potential differences in the biotic impact of thermogenic gas release versus volcanic outgassing.

Volcanoes represent a major source of mercury (Hg) in the natural environment. Anomalous Hg enrichments in sedimentary rocks are now

* Corresponding author.
E-mail address: davidkemp@cug.edu.cn (D.B. Kemp).

https://doi.org/10.1016/j.epsl.2023.118438
Received 26 June 2023; Received in revised form 29 September 2023; Accepted 10 October 2023
Available online 25 October 2023
0012-821X/© 2023 Elsevier B.V. All rights reserved.

widely used as a proxy for large-scale paleovolcanism, and have the potential to establish temporal links between magmatism, extinction and large-scale carbon release (Grasby et al., 2019; Jin et al., 2023; Shen et al., 2023; Svensen et al., 2023). Enrichments in sedimentary Hg have been recorded broadly coincident with the ETME (Thibodeau et al., 2016; Percival et al., 2017; Lindström et al., 2019; Ruhl et al., 2020; Yager et al., 2021; Shen et al., 2022a, 2022b). Nevertheless, Hg abundance data alone may offer only limited insights into the source and volume of emissions (though see Fendley et al., 2019 for an important exception). In particular, sedimentary Hg abundance can be complicated by host phase mineral/component variations, source changes, and post-depositional degradation (Hammer et al., 2019; Charbonnier et al., 2020; Shen et al., 2020; Park et al., 2022).

Hg isotopes potentially offer a more robust understanding of Hg sources. Specifically, mass-independent fractionation (MIF) of odd Hg isotopes (expressed in delta notation as Δ^{199}Hg) can reflect the pathways of Hg entering the sedimentary environment and has distinctive values in different reservoirs. Notably, Δ^{199}Hg values of near-zero may characterize large igneous province (LIP) emissions sourced from the primitive mantle (Yin et al., 2022), while terrestrial and atmospheric fluxes are normally characterized by negative and positive values, respectively (Blum et al., 2014). Because odd-MIF of Hg is largely stable during physical, chemical and biological processes other than photochemical reactions, and because there is no odd-MIF recorded during host phase transitions and diagenesis, sedimentary records of Hg-isotopes have provided insights into the sources of Hg during the ETME (Thibodeau et al., 2016; Yager et al., 2021; Shen et al., 2022a, 2022b). Specifically, near-zero Δ^{199}Hg (i.e. negligible MIF) across the ETME in globally distributed shallow marine sections are interpreted as evidence for a predominantly volcanogenic source of Hg (Thibodeau et al., 2016; Yager et al., 2021). However, recent observations of negative Δ^{199}Hg values across the ETME from the deep ocean emphasize spatial variability in Hg-isotope patterns, and the likely importance of Hg sourced from organic matter combustion linked to volcanism (Shen et al., 2022a). The observed spatial heterogeneity of Hg-isotopes in sedimentary records, linked in part to transport distances (Shen et al., 2022a), complicates interpretation of global Hg source variations and volcanogenic fluxes across the ETME. Equally, other non-volcanic factors (such as terrestrial biomass and flux changes linked to warming) may also complicate ETME Δ^{199}Hg signals.

In this study, we present new Hg-isotope and associated geochemistry data from a biostratigraphically well-constrained sedimentary succession across the ETME in southwest England at St Audrie's Bay (Bristol Channel Basin, Fig.1), deposited close to the CAMP. Different factors (i.e. exogenic input vs. local flux change) that may have driven Δ^{199}Hg variations in this section are assessed, and quantitatively evaluated using a simple mass balance model. The relative timing of different styles of CAMP magmatism are inferred from the data, and evaluated based on the likely stratigraphic correlation between the data and other records of the ETME and end-Triassic magmatism.

2. Geological setting and the ETME at St. Audrie's Bay

The St Audrie's Bay section (southwest England, 51.182°N, 3.286°W; Fig. 1) was deposited in an epicontinental area and spans the Norian-Rhaetian to the Hettangian. Relative sea level and depositional environments varied throughout the section. The Blue Anchor Formation is characterized by mudstones/dolostones with occasional evaporitic features likely deposited in a hypersaline lake/ephemeral playa environment (Warrington and Whittaker, 1984). The environment transitioned to a marine setting towards the top of the Blue Anchor Formation (Williton Member), with restricted marine conditions with storm influence developed in the overlying Westbury Formation mudstones (MacQuaker, 1987). Above the Westbury Formation, the lower Cotham Member of the Lilstock Formation was deposited in shallow marine conditions, with the upper Cotham Member marking the onset of a transgression into marine limestone and mudstones of the Langport Member (Hesselbo et al., 2004). The overlying shales, marls and limestones of the Blue Lias Formation were deposited in deeper fully marine conditions under ephemeral anoxic/euxinic conditions (Hesselbo et al., 2002; He et al., 2022).

Due to the lack of the typical Triassic ammonoid *Choristoceras marshi* and the Jurassic ammonite *Psiloceras spelae*, the ETME interval at St Audrie's Bay is not well established and relies on $\delta^{13}C_{org}$ correlation (Hillebrandt et al., 2013). Negative CIEs across the ETME interval (i.e. 'Initial CIE' and 'Main CIE' in Hesselbo et al., 2002; 'Marshi CIE', 'Spalae CIE' and 'top-Tilmanni CIE' in Lindström et al., 2017, 2021) have been linked to voluminous emission of ^{13}C-depleted carbon associated with magmatism. Hesselbo et al. (2002) recognized a sharp CIE in the Lilstock Formation (Initial CIE, known as the Spalae CIE in Lindstrom et al., 2021) and suggested that this marks the onset of major basaltic volcanism from CAMP and floral and faunal turnover (Fig. S1). More recently,

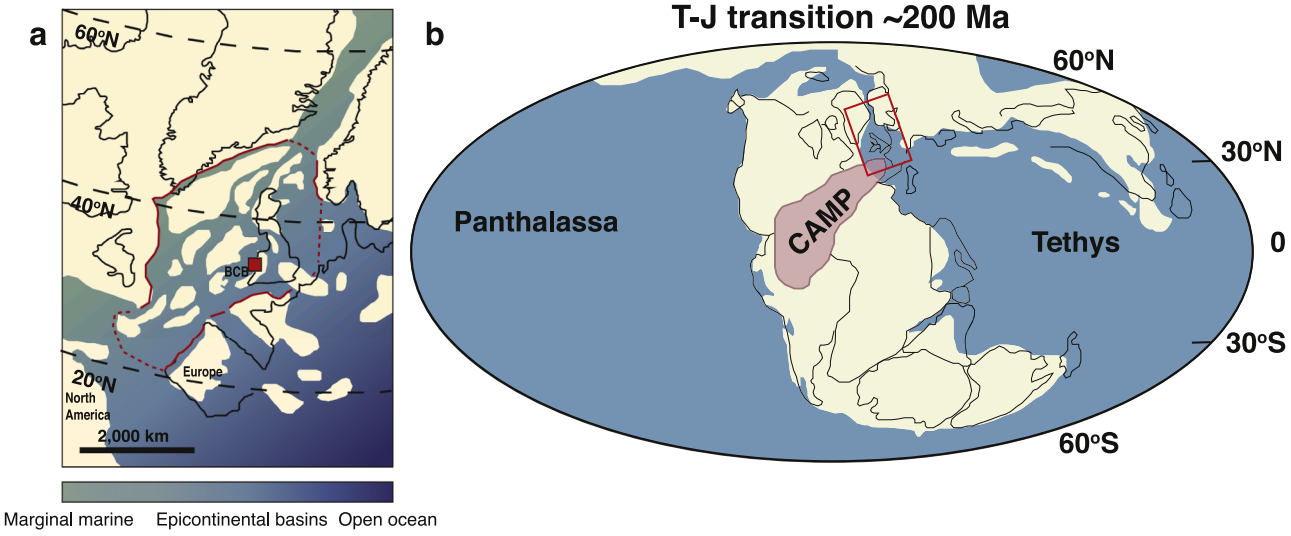

Fig. 1. Paleogeography and location of the studied St Audrie's Bay section. a, Paleogeographic map of the European seaway. BCB: Bristol Channel Basin. Red rectangle shows the location of St Audrie's Bay. Red lines denote the approximate boundary of the European seaway (used for mass balance calculations in main text). **b**, Global paleogeographic reconstruction for the Triassic-Jurassic, with the location of the Central Atlantic Magmatic Province (CAMP) highlighted. Modified from He et al. (2022), with paleogeographic location and extent of CAMP based on Marzoli et al. (2018).

it has been shown that the Initial CIE at St. Audrie's Bay likely orginates from a change in organic matter source linked to sea level/environmental change, and not from an exogenic input of ^{12}C-enriched volcanic carbon (Fox et al., 2020). In addition, a newly established ETME correlation scheme using abundance of *P. polymicroforatus* across NW Europe suggests that the major marine invertebrate extinctions and terrestrial ecosystem changes took place prior to the Initial/Spalae CIE at St Audrie's Bay (40.85 m), and the base of the ETME may correlate to an excursion named the Marshi CIE, which is tentatively recognised in the Westbury Formation (35.85 m, Bonis et al., 2010; Lindström et al., 2012, 2017, 2021; Fig. 4). The Marshi CIE may coincide with the major intrusive phase of CAMP (Lindström et al., 2017, 2021; Fig. 4).

3. Materials and methods

A total of 100 samples were collected across a 49.1 m interval spanning the Blue Anchor Formation to the Blue Lias Formation at St Audrie's Bay section. Samples were dried and ground to 200 mesh for subsequent geochemical analysis.

3.1. Element and total organic carbon concentrations

All 100 samples were analysed for Hg concentration using a Milestone DMA-80 Evo at the School of Earth Sciences, China University of Geosciences (Wuhan). 70 ± 5 mg of dry and powered whole rock sample was weighed out and the precise mass was recorded. The material was heated to 1000 °C under oxygen flow to be thermally decomposed. Mercury species were then catalysed to be reduced and trapped on a gold amalgamator followed by subsequent release and measuring. A soil Reference Standard (GBW07423, 32 ± 3 ng/g Hg) was analyzed after every ten samples to monitor accuracy. Analytical precision based on these standards was better than ± 2.44 ng/g (2σ).

Samples were analyzed for total organic carbon (TOC) using a Vario EL Cube elemental analyser at the Faculty of Materials Science and Chemistry, China University of Geosciences (Wuhan). For each sample, approximately 1 g of dried powdered rock was digested in 2 M HCl for at least 24 h to remove carbonate minerals. After drying at 45 °C, samples were loaded into tin capsules ready for measurement. Carbonate content was determined by the mass percentage loss during decalcification. Sulfanilamide was used as a calibration standard, and analytical precision was better than ± 0.06 wt% (2σ).

Samples were analyzed for sulfide concentration using a LECO CS844 instrument by ALS Chemex (Guangzhou) Co., Ltd. A sodium carbonate leach was used to remove sulfate, and the insoluble sulfide residue was filtered and analysed. Analyses of standards OREAS −45e, OREAS −72a, OREAS −74a yielded analytical precision better than ± 0.02% (2σ).

Samples were analyzed for Al using an Agilent-5110 ICP-OES by ALS Chemex (Guangzhou) Co., Ltd. A four-acid digestion method of HNO_3–$HClO_4$–HF–HCl was conducted in three steps to dissolve most of the minerals. HNO_3 and $HClO_4$ were firstly used for pre-oxidation followed by addition of HF for digestion of silicate and aluminate. The solution was then evaporated and HCl was added before measurements. Multiple replicate analyses of one sample and standards yielded analytical precision better than ± 0.42% (2σ).

3.2. Hg isotopes

A subset of 26 samples was analyzed for Hg isotopes at the State Key Laboratory of Environmental Geochemistry, Institute of Geochemistry, Chinese Academy of Sciences, Guiyang. Hg preconcentration was proceeded by a double-stage tube furnace coupled with 40% (HNO_3/HCl = 2/1, v/v) trapping solution (Huang et al., 2015). This method, which enables a complete release of Hg from samples under 850 °C and an efficient capture of the released Hg in the trapping solution, yielded good Hg recoveries of 90 to 110% for the samples, avoiding any potential Hg isotope fractionation during sample processing. The trapping solutions were then diluted to ~0.5 ng/mL Hg in 10–20% (v/v) acids using Milli-Q water, and analyzed using a Neptune Plus multiple collector inductively coupled plasma mass spectrometer (Thermo Electron Corp, Bremen, Germany), following a previous method (Yin et al., 2016a). Hg isotope results are expressed as delta (δ) values in units of per mille (‰) relative to the bracketed NIST 3133 Hg standard, as follows:

$$\delta^{202}\mathrm{Hg} = \left[\left(^{202}\mathrm{Hg}/^{198}\mathrm{Hg}\right)_{\mathrm{sample}} \Big/ \left(^{202}\mathrm{Hg}/^{198}\mathrm{Hg}\right)_{\mathrm{standard}} - 1\right] \times 1000$$

MIF values were calculated for ^{199}Hg and ^{200}Hg, and expressed as per mille deviations from the predicted values based on the mass-dependent fractionation (MDF) law (Bergquist et al., 2007):

$$\Delta^{199}\mathrm{Hg} = \delta^{199}\mathrm{Hg} - 0.2520 \times \delta^{202}\mathrm{Hg}$$
$$\Delta^{200}\mathrm{Hg} = \delta^{200}\mathrm{Hg} - 0.5024 \times \delta^{202}\mathrm{Hg}$$

Standard reference materials (GSS-4, soil) were prepared and measured in the same way as the samples. NIST-3177 secondary standard solution, diluted to 0.5 ng/mL Hg, was measured in every 5 to 10 samples. Analytical uncertainty was estimated based on replicate analyses of the NIST-3177 secondary standard solution and GSS-4 (±0.1‰, ±0.04‰ and ±0.06‰, 2σ for δ^{202}Hg, Δ^{199}Hg and Δ^{200}Hg, respectively).

To obtain our final Hg isotope record, the data measured in this study are integrated with the previously published Hg isotope data from Yager et al. (2021) according to lithostratigraphic (bed by bed) correlation.

3.3. Organic geochemistry

A subset of 32 samples were prepared and measured for n-alkane, pristane and phytane content at State Key Laboratory of Biogeology and Environmental Geology, China University of Geosciences (Wuhan). Powdered rock samples (ca. 20–40 g) were extracted for bitumen compounds using a 9:1 dichloromethane:methanol (DCM:MeOH, v/v) solution in an accelerated solvent extractor (ASE 150, Dionex) at a pressure of 1500–1600 Pa and a temperature of 100 °C, with extractions proceeding through 3 cycles of 15 min cycle^{-1}. Activated copper turnings (sonicated for 30 mins in 2 M HCl, brought to a neutral pH using ultrapure water, cleaned using 9:1 DCM:MeOH, v/v) were used to remove elemental sulfur. After solvent removal under reduced pressure, the extract was fractionated into saturate fraction (n-hexane) using silica gel column chromatography. The n-alkane analyses were carried out using an Agilent 8890 gas chromatograph (GC) with helium as carrier gas, equipped with a Rtx-5 column (30 m × 0.25 mm) and a flame ionization detector (FID). The oven temperature was programmed from 70 °C to 210 °C at 10 °C/min, then to 300 °C at 3 °C/min and held for 30 mins. An internal standard of cholestane was used for correction of quantitative analyses. The carbon preference index (CPI), average chain length (ACL), terrestrial aquatic ratio (TAR) were based on the relative abundance of the long chain n-alkanes, according to the following equations (Poynter and Eglinton, 1990; Peters et al., 2005):

$$\mathrm{CPI} = 0.5 \times [([C_{25}] + [C_{27}] + [C_{29}] + [C_{31}] + [C_{33}])/([C_{24}] + [C_{26}] + [C_{28}] + [C_{30}] + [C_{32}]) + ([C_{25}] + [C_{27}] + [C_{29}] + [C_{31}] + [C_{33}])/([C_{26}] + [C_{28}] + [C_{30}] + [C_{32}] + [C_{34}])]$$

$$\mathrm{ACL} = (25 \times [C_{25}] + 27 \times [C_{27}] + 29 \times [C_{29}] + 31 \times [C_{31}] + 33 \times [C_{33}])/([C_{25}] + [C_{27}] + [C_{29}] + [C_{31}] + [C_{33}])$$

$$\mathrm{TAR} = ([C_{27}] + [C_{29}] + [C_{31}])/([C_{15}] + [C_{17}] + [C_{19}])$$

3.4. Mass balance calculation

A mass balance equation is used to evaluate the mass of Hg of a given isotopic composition needed to drive changes in Δ^{199}Hg. The equations are modified from McInerney and Wing (2011):

$$M_{added} = M_{initial} \times (\Delta^{199}Hg_{initial} - \Delta^{199}Hg_{final})/(\Delta^{199}Hg_{final} - \Delta^{199}Hg_{added}),$$

$$M_{subtracted} = M_{initial} \times (\Delta^{199}Hg_{final} - \Delta^{199}Hg_{initial})/(\Delta^{199}Hg_{final} - \Delta^{199}Hg_{subtracted}),$$

where $M_{initial}$ is the Hg reservoir size, $M_{added/substracted}$ is the mass of Hg added into/substracted from a given reservoir, $\Delta^{199}Hg_{initial}$ is the value prior to the positive/negative $\Delta^{199}Hg$ shift, and $\Delta^{199}Hg_{final}$ is the final value of the positive/negative shift. $\Delta^{199}Hg_{added/substracted}$ is the isotopic composition of the Hg source causing the isotopic shift.

Due to the short residence time of Hg in the ocean relative to the timescale of ocean circulation (Zhang et al., 2014; see also Results and Discussion 4.2), the mass balance model may be suitable for constraining local to regional scale changes. The natural global ocean Hg reservoir size before significant anthropogenic influence was estimated as 1.22×10^5 to 1.98×10^5 Mg (total of surface, intermediate and deep ocean; Amos et al., 2013). The areal extent of the Bristol Channel Basin and European seaway, as a proportion of the global ocean, is estimated as ~0.01% and 1%, respectively, using a global paleogeographical basemap (Scotese et al., 2014). Assuming the near-shore Bristol Channel Basin is composed of surface ocean water (e.g., <50 m), the Hg reservoir size ($M_{initial}$) of the Bristol Channel Basin is estimated as ~5.6 Mg considering enhanced terrestrial input in a near-shore environment (i.e. the riverine Hg concentration into the modern North Atlantic ocean of ~9.1 pM in Amos et al., 2014), and a total global surface ocean volume of 3.07×10^{16} m^3. The $M_{initial}$ of the European Seaway (1 % of the global ocean reservoir) is estimated to be ~1.23×10^3 to 2.01×10^3 Mg Hg.

The $\Delta^{199}Hg$ values of various Hg sources are not well-constrained. For volcanically sourced Hg outgassed from effusive eruption, we use $\Delta^{199}Hg = 0.02 \pm 0.06$‰ (Yin et al., 2016b). For terrestrially sourced Hg, we assume $\Delta^{199}Hg = -0.6 \pm 0.04$‰ based on the average of the lowest 5 $\Delta^{199}Hg$ values in the predominantly terrestrial Blue Anchor Formation (Fig. 2). The same terrestrial value is used to represent thermogenically sourced Hg outgassed via contact metamorphism of organic-rich sediments (broadly consistent with Yin et al., 2016b, i.e. median = –0.32‰, range: –0.65 to 0.1‰ for terrestrial plants).

4. Results and discussion

4.1. Hg, Hg-isotopes and host phase transitions through the Late Triassic to Early Jurassic at St. Audrie's Bay

Total Hg concentrations range from 0 to 233 ng/g (mean = 41.3 ng/g) through the St. Audrie's Bay succession, which spans from the Norian (Late Triassic) through to the Hettangian (Early Jurassic) (Fig. 2). Hg is relatively elevated and variable (0 to 233 ng/g, mean = 49.4 ng/g) within the predominantly non-marine Blue Anchor Formation at the base of the succession (2.1 to 30.5 m). By contrast, Hg is lower and less variable upwards through the succeeding marine Westbury, Lilstock and Blue Lias Formations (30.5 to 45.85 m, 5 to 77 ng/g, mean = 35.8 ng/g), which encompass the ETME interval (~35.1 to 42.1 m in the upper part of the Westbury Formation and Lilstock Formation based on correlation of Lindström et al., 2017, 2021; see also Fig. 4).

The $\delta^{202}Hg$ values range from –1.62‰ to +0.35‰ (mean = –0.82‰, augmented with data from Yager et al., 2021; Fig. 2) across the section. Given that the variation of $\delta^{202}Hg$ can result from mass-dependent fractionation (MDF) during numerous biological, abiotic chemical and physical processes, it is difficult to directly link $\delta^{202}Hg$ changes to Hg source variations (Blum et al., 2014). $\Delta^{199}Hg$ (augmented with data from Yager et al., 2021; Fig. 2) vary from –0.62 to –0.07‰. Mean $\Delta^{199}Hg$

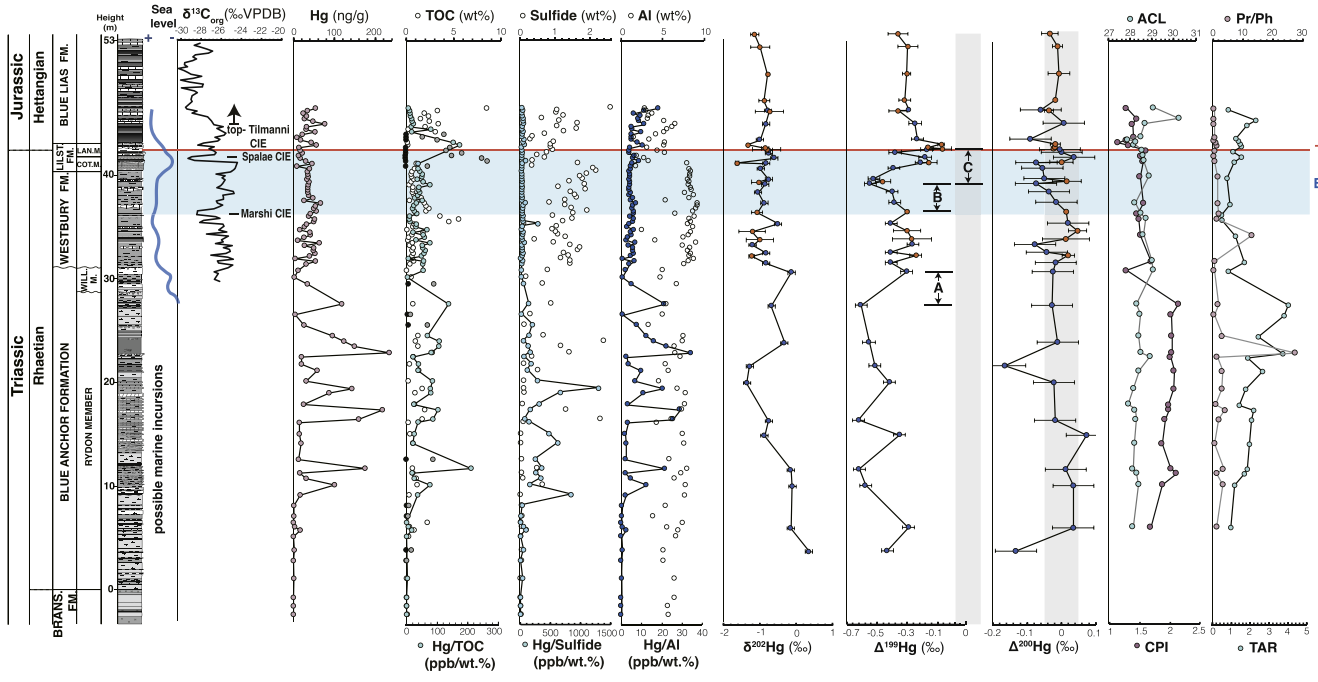

Fig. 2. Stratigraphic changes in Hg and Hg-isotopes and key geochemical data at St. Audrie's Bay. Major Hg host phases (TOC, sulfide, and Al – a proxy for clay), and selected biomarker indices are shown. The gray bar in the $\Delta^{199}Hg$ column is the assumed volcanic value of 0.02 ± 0.06‰ (Yin et al., 2016b), and the gray bar in the $\Delta^{200}Hg$ column represents values of 0 ± 0.05‰ without significant fractionation (Yin et al., 2016b). Black-filled dots in TOC column are TOC values <0.2 wt.%, and gray-filled dots in Hg/TOC column are those datapoints with TOC values <0.2 wt.%. Hg isotopic data from (Yager et al., 2021) and this study are colored orange and blue, respectively. $\Delta^{199}Hg$ shifts A, B, C indicate a + 0.3‰ shift at 27.3–30.5 m, a –0.25‰ shift at 36.2–38.85 m, and a + 0.48‰ shift at 38.85 to 42.2 m, respectively (see main text for discussion). Relative sea level curve is from Hesselbo et al. (2004). Organic carbon isotope data ($\delta^{13}C_{org}$) are from Hesselbo et al. (2002). Definitions of ETME interval and TJB follow Lindström et al. (2017, 2021). Sedimentary log of the Westbury Formation and higher is from Hesselbo et al. (2002). Log of the Blue Anchor Formation is from this study. CIE: carbon isotope excursions; CPI: Carbon preference index; ACL: Average chain length; TAR: terrestrial-aquatic ratio; Pr/Ph: pristine/phytane ratio.

is –0.48‰ within the Blue Anchor Formation, with a ~+0.3‰ shift across the boundary between the non-marine Rydon Member and marine Williton Member (Shift A, 27.3 to 30.5 m; Fig. 2). Near the top of the Westbury Formation (36.2 m) there is a –0.25‰ decrease spanning 2.65 m (Shift B), followed by a + 0.48‰ increase spanning 3.35 m across the uppermost Westbury Formation and Lilstock Formation (Shift C, 38.85 to 42.2 m). Δ^{199}Hg values are broadly stable and negative above this in the Blue Lias Formation (mean = –0.3‰). Even-MIF (i.e. Δ^{200}Hg) can be largely controlled by photochemical reactions in the atmosphere. Atmospheric samples that contain photoxidized Hg(II) species and gaseous Hg(0) are characterized by positive and negative values (Gratz et al., 2010; Zerkle et al., 2020), which are followed by wet and dry deposition respectively into sediments. Δ^{200}Hg values are broadly consistent and close to zero, within uncertainty (±0.06‰, 2σ), ranging from –0.16‰ to 0.07‰ (mean = –0.02‰) prior to ETME (–2.1 m to 35.1 m), and from –0.09‰ to 0.04‰ (mean = –0.02‰) during and after ETME (35.1 m to 53.1 m; Fig. 2).

Hg is hosted in sediments and sedimentary rocks by different mineral phases and components; typically organic matter and sulfide, though clay minerals can also (more rarely) be an important host phase (Grasby et al., 2019; Shen et al., 2020). Within the Blue Anchor Formation, Hg correlates most strongly with total organic carbon (TOC) content (Pearson $r = 0.85$, $p < 0.01$, $n = 39$), and with aluminum (Al) (a proxy for clay content) within the Westbury and Lilstock Formations ($r = 0.63$, $p < 0.01$, $n = 37$ and $r = 0.72$, $p = 0.02$, $n = 10$, respectively) (Figs. 2; S2; Table S1). Hg correlates most strongly with sulfide content in the Blue Lias Formation ($r = 0.68$, $p = 0.014$, $n = 12$) (Figs. 2; S2; Table S1). The varying strength of the correlations between Hg and candidate host phases in the different formations suggests host phase transitions through the section (see also Fig. S2 and Table S1). Based on the correlations, Hg is likely hosted primarily in organic matter in the Blue Anchor Formation, primarily in clays in the Westbury and Lilstock Formations, and primarily in sulfides in the Blue Lias Formation. Our finding that Hg is hosted in clays and sulfides in the Lilstock-Blue Lias

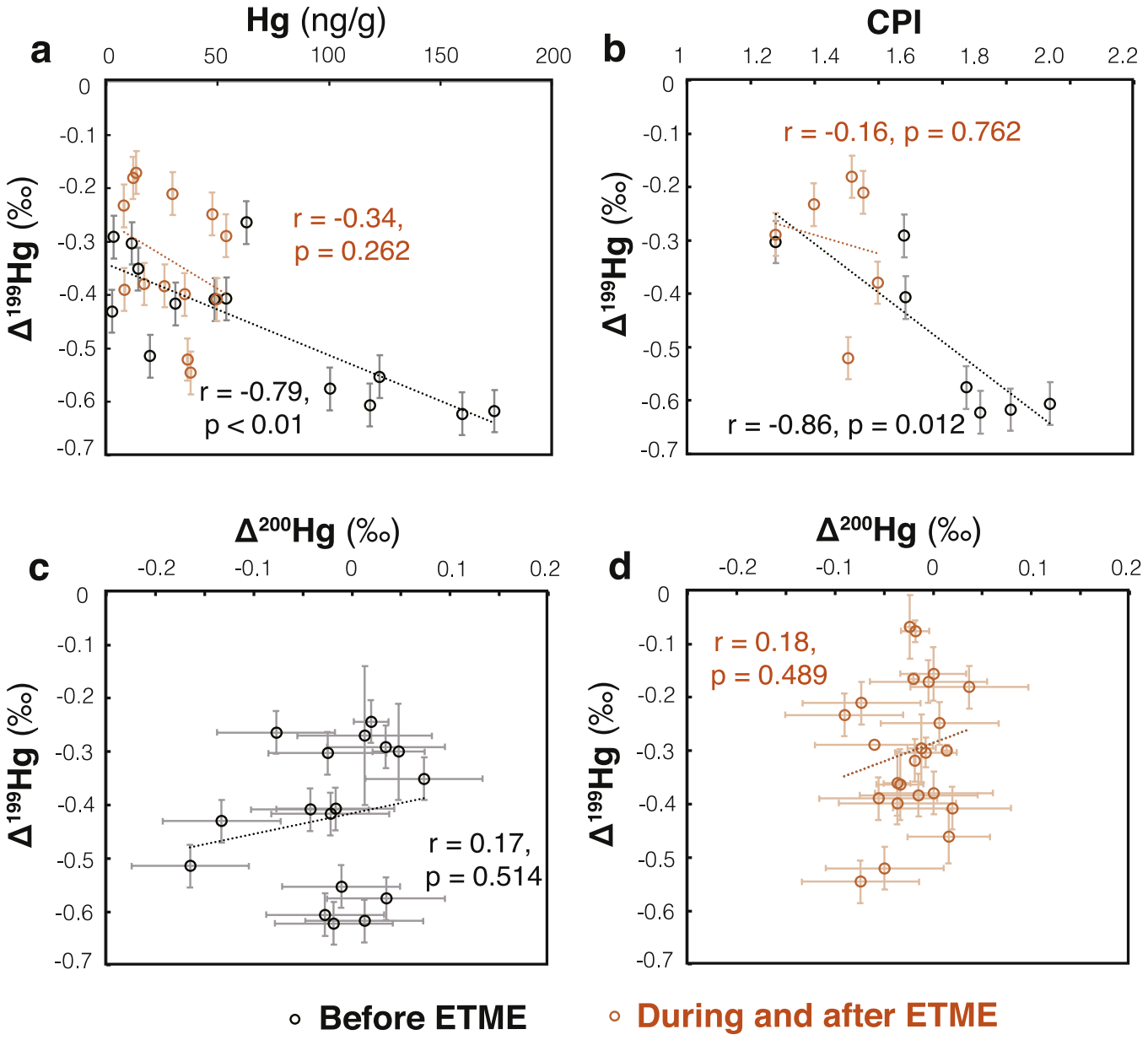

Fig. 3. Correlations (Pearson *r* values and associated *p* values) between Hg and various geochemical data before, and during/after ETME. a, Δ^{199}Hg – Hg, **b**, Δ^{199}Hg – CPI (carbon preference index), **c** and **d**, Δ^{199}Hg – Δ^{200}Hg. Data are split into those before the ETME (black data) and those during/after the ETME (orange data). Error bars for Δ^{199}Hg and Δ^{200}Hg are the 2σ errors.

interval contrasts with previous works (Percival et al., 2017; Yager et al., 2021), which assumed an organic matter host of Hg (and did not present Al and sulfide data). Indeed, the Hg/TOC enrichment across the ETME (40.85 to 43.1 m) in the Lilstock Formation and the lowermost part of the Blue Lias Formation previously observed (Percival et al., 2017; Yager et al., 2021; also apparent in our data, Fig. 2) is mainly attributable to low TOC (mean = 0.15 wt.% between 40.85 m and 43.1 m), which sensitises Hg/TOC to small changes in TOC (Grasby et al., 2019). This is further exacerbated by dilution of TOC by carbonate content, which is relatively high in the Lilstock Formation (Fig. S2). Normalized to Al and sulfide abundance, Hg shows no anomalous enrichment across the ETME interval (Fig. 2). Nonetheless, the relatively high Al and sulfide contents during the ETME (mean = 7.19 and 1.33 wt.%, respectively, Fig.2) could contribute to the low Hg/host ratio. Taken together, evidence for CAMP volcanism from the Hg concentration data alone is unclear.

The lowest Δ^{199}Hg values occur in the predominantly non-marine Blue Anchor Formation, and Hg enrichment spikes in this formation are typically coincident with the most negative Δ^{199}Hg values (Hg–Δ^{199}Hg correlation $r = -0.79$, $p < 0.01$; Fig. 3a). We also note a strong negative correlation between Δ^{199}Hg and carbon preference index (CPI, $r = -0.86$, $p = 0.012$) through the succession prior to the ETME interval (Fig. 3b). CPI reflects the predominance of odd-over-even n-alkane chain lengths, with odd-numbered chain lengths predominating (CPI >1) in immature terrestrial organic matter (Bray and Evans, 1961; Peters et al., 2005). As such, the data emphasize an organic matter source control on Δ^{199}Hg. This is most clearly emphasized by the increase in Δ^{199}Hg (~+0.31‰) at Shift A near the top of the Blue Anchor Formation (Rydon-Williton Member boundary, Fig. 2), which is coincident with reduced terrestrially sourced organic matter, as indicated by decreasing CPI and TAR and the transition from terrestrial to marine conditions. Taken together, organic matter type strongly controls Δ^{199}Hg values prior to ETME.

4.2. *Evidence for thermogenic and volcanogenic Hg release during the ETME*

Although Hg abundance data do not provide clear evidence of volcanic input of Hg to the environment across the ETME at St. Audrie's Bay, previous Hg-isotope data across this interval have indicated a likely pulse of volcanic Hg (Yager et al., 2021). Our new higher resolution and extended Δ^{199}Hg record allows us to evaluate this previous deduction in detail. In contrast to the data below the ETME, Δ^{199}Hg shifts B and C in the ETME interval are not associated with changes in CPI, TAR or any other proxy for organic matter type (Fig. 2). There is no significant correlation between Δ^{199}Hg and CPI ($r = -0.16$, $p = 0.762$) within and above the ETME (Fig. 3b). Together with the fact that the Hg host phase transitioned to clays/sulfide during the ETME and above, the decoupling between organic matter type and Δ^{199}Hg strongly suggests that the Hg was no longer largely associated with organic matter binding, and thus not significantly influenced by organic matter source changes. As such, shifts B and C in the ETME were likely to have been driven by an exogenic input of Hg.

A plausible major source of Hg with relatively low Δ^{199}Hg that could have driven the negative shift in Δ^{199}Hg at shift B is thermogenic Hg emitted during magma intrusion into organic-rich sediment (Heimdal

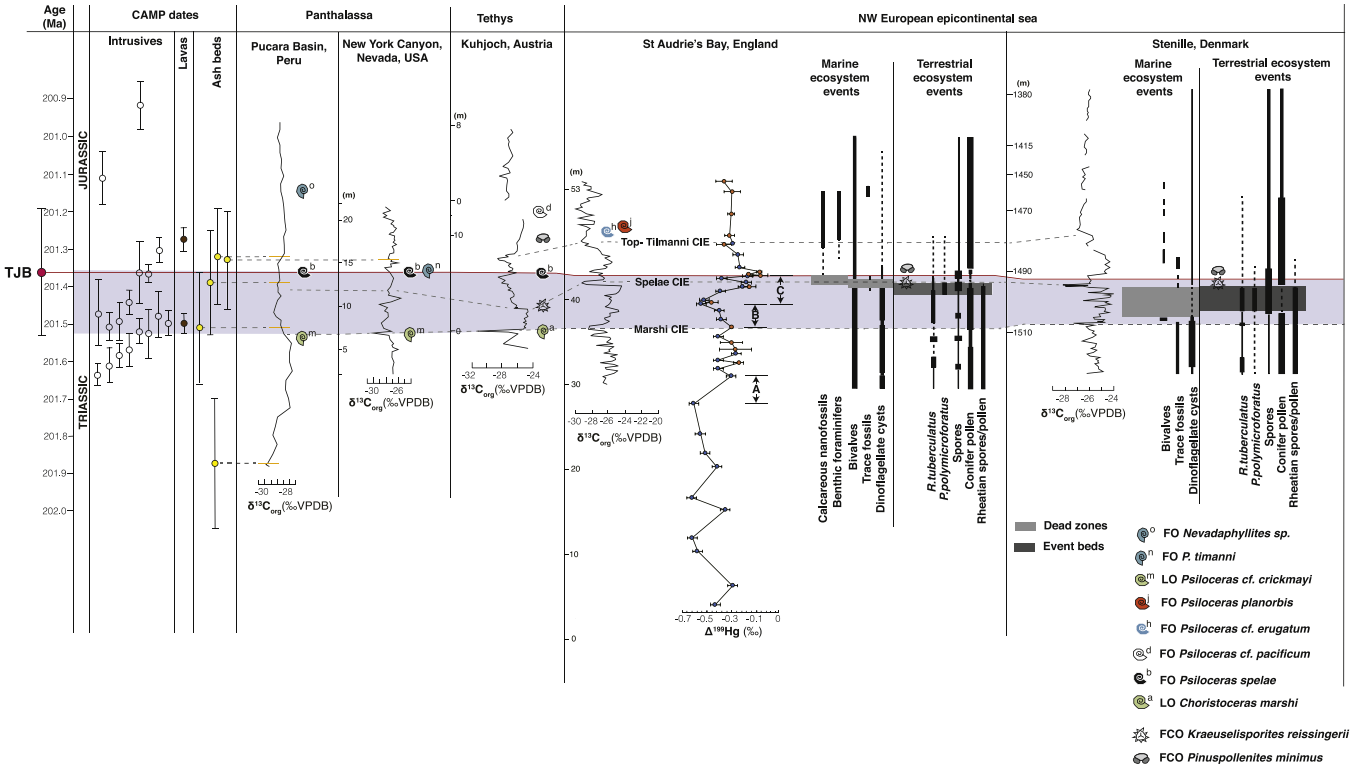

Fig. 4. Synthesis of CAMP intrusion and ash bed ages, plotted against ETME data and carbon and Hg isotope data. Correlations of CAMP ages to global sections and $\delta^{13}C_{org}$ data are based on Lindström et al. (2021). Geochronology of CAMP intrusions and lava flows are from Blackburn et al. (2013), Davies et al. (2017), Heimdal et al. (2018), and Marzoli et al. (2019). Geochronology of ash beds is from the ammonoid bearing successions in Nevada, USA (Schoene et al., 2010) and the Pucara Basin, Peru (Schoene et al., 2010; Wotzlaw et al., 2014). Short horizontal orange lines mark the stratigraphic levels of U-Pb dated ash beds on the carbon isotope curves at Nevada and Peru. The ETME is defined as the interval between the LO of *C.crickmayi* or *C. marshi* and the FO of *P. spelae* (Hillebrandt et al., 2013), and is marked with purple shading. Vertical axis of Pucara Basin section data is in time. Extinction events at St. Audrie's Bay and Stenille (Denmark) are from Lindström et al. (2012). The TJB is defined by the first occurrence (FO) of *Psiloceras spelae*, marked by a red line, estimated at 201.36 ± 0.17 Ma (Wotzlaw et al., 2014). $\delta^{13}C_{org}$ records are from Pucara Basin (Yager et al., 2017), Nevada (Guex et al., 2004), Kuhjoch (Ruhl et al., 2009), St Audrie's Bay (Hesselbo et al., 2002) and Stenille (Lindström et al., 2012). Figure is modified from Lindström et al. (2012, 2017, 2021).

et al., 2018; Shen et al., 2022a; Svensen et al., 2023). Synchronicity between the timing of CAMP intrusives and shift B is supported by the available correlations to CAMP intrusion ages (Lindström et al., 2017, 2021; Fig. 4). Specifically, the correlation scheme of Lindstrom et al. (2017, 2021) implies that Shift B is coeval with a cluster of U-Pb intrusion dates (Fig. 4). Even if Shift B was older (as originally implied by Hesselbo et al., 2002, Fig. S1, see also Section 2), then it would still be broadly coincident with intrusion. During this major phase of CAMP activity, sills intruded into Devonian-Carboniferous rocks, including organic-rich shales across Africa, North America and Europe, and especially Brazilian basins in South America (Marzoli et al., 2018). The release of volatiles (i.e. Hg, CO_2, CH_4) during this contact metamorphism has been proposed previously (Heimdal et al., 2018; Capriolo et al., 2021; Shen et al., 2022a).

Evaluating the precise masses of thermogenic Hg required to drive shift B is complicated by the short residence time of Hg in seawater (a few months in the surface ocean and hundreds of years in the intermediate ocean, Zhang et al., 2014). This residence time is less than the timescale of global oceanic circulation (~10^3 yrs). Therefore, sedimentary Hg isotopes from marine records represent only regional or basin-scale signals, contributing to the observed heterogeneity in global Hg isotope records across the ETME (Yager et al., 2021; Shen et al., 2022a, 2022b).

Assuming the Hg isotope signal at St. Audrie's Bay reflects a basin-scale signal that tracks CAMP activity, a simple mass balance can be used to illustrate the mass of thermogenic Hg (i.e. Δ^{199}Hg = –0.6 ± 0.04‰) needed to drive the –0.25‰ magnitude shift B (assuming no source mixing or source change) (Section 3.4). Based on the estimated Hg reservoir size of ~5.6 Mg in the Bristol Channel Basin (see Section 3.4), ~28 Mg of thermogenic Hg would be required to drive the shift (Fig. 5a). If Shift B was representative of the entire European seaway (~1230.9 to 2008.5 Mg Hg; see Section 3.4), then 6.15×10^3 to 1×10^4 Mg of thermogenic Hg would be required to drive it (Fig. 5a). The release of up to 9.92×10^5 Mg of thermogenic Hg to drive Shift B at a global scale (Fig. 5a) implies an associated release of carbon that is well within the previously estimated thermogenic carbon emission masses quantified from CAMP intrusive rocks (see Supplementary Information).

Following Shift B, the marked +0.48‰ Δ^{199}Hg change at Shift C was previously noted by Yager et al. (2021), and suggested by them to have been caused by direct volcanic emission of Hg. Assuming this volcanic Hg had a Δ^{199}Hg value of +0.02‰ (see Section 3.4), our mass balance model suggests that within the Bristol Channel Basin alone, Shift C could have been driven by the release of ~29.9 Mg of volcanic Hg (Fig. 5b). If Shift C was representative of the entire European seaway or global ocean, then it would require 1.07×10^4 Mg or 1.06×10^6 Mg Hg, respectively. As for Shift B, the implied volumes of carbon release associated with these Hg masses are well within likely volume ranges of CAMP basalts (See Supplementary Information).

There are several important caveats to these calculations. Intrusive and extrusive activity almost certainly co-occurred for much of CAMP (as indicated by overlapping intrusion and ash-bed dates, for example; Fig. 4), and the mass balance calculations solely consider a single source of Hg during each shift. As already noted (Section 3.4), end-member Δ^{199}Hg values for thermogenic and volcanic Hg are poorly known, as are pre-Anthropocene reservoir masses. Moreover, because the minimum Δ^{199}Hg values reached at shifts B and C are close to the end-member values used in the mass balance, the masses calculated represent likely minimum estimates (Fig. S3). For a comparison, we used our mass balance calculation to evaluate the Δ^{199}Hg data from New York Canyon, Nevada, which was deposited in a mid-inner shelf environment in Panthalassa (Thibodeau et al., 2016). The amount of volcanogenic Hg required to drive the observed 0.13‰ positive Δ^{199}Hg shift across the ETME in this section is comparable with our estimate for the Bristol Channel Basin (~2.00×10^2 Mg Hg), considering an assumed larger Hg reservoir size at New York Canyon (13.9 Mg) (see Supplementary Information).

The relatively low calculated masses of Hg required to drive the Hg-isotope shifts, despite the likely larger masses released from CAMP, may relate to its rapid (~1 year) cycling (Selin, 2009), which could limit the mass of Hg reaching the basins (St Audrie's Bay was paleogeographically ~1000–2000 km from outcrops of CAMP volcanics). It is also worth noting that our calculations do not take into account changes in Δ^{199}Hg caused by this atmospheric transport (Shen et al., 2022a). This would shift Δ^{199}Hg to more positive values via photoreduction (Blum et al., 2014). We note that although even-MIF (i.e. Δ^{200}Hg) can be largely controlled by photochemical reactions in the atmosphere (Zerkle et al., 2020; Gratz et al., 2010), the Δ^{200}Hg mean value of −0.03‰ and the insignificant correlation between Δ^{199}Hg and Δ^{200}Hg at St Audrie's Bay

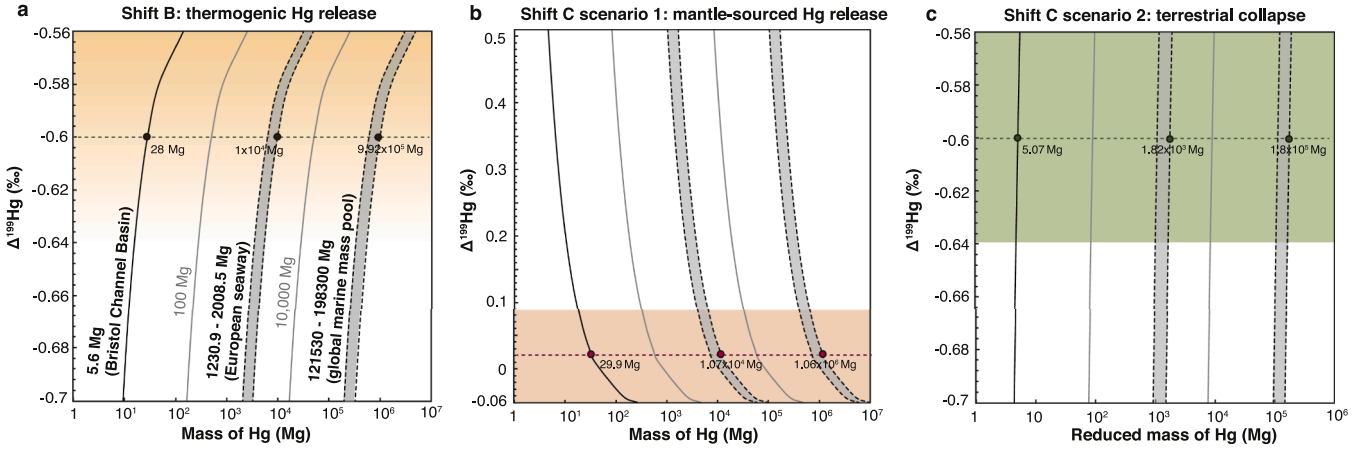

Fig. 5. Mass balance constraints on Hg volumes required to drive observed shifts in the Δ^{199}Hg record at St. Audrie's Bay. Calculations are made assuming the changes reflect either local basin-scale, regional (seaway-scale), or global-scale changes. For mass balance equations and further information see main text. **a**, Masses of Hg need to drive Shift B via thermogenic Hg release from intrusive heating of organic-rich sedimentary rocks. **b**, Masses of Hg required to drive Shift C via Hg release from CAMP volcanoes (Scenario 1). **c**, Decreases in terrestrial Hg (expressed as masses) required to drive Shift C assuming terrestrial collapse and consequent reduction in terrestrial Hg input (Scenario 2). Colored bars indicate Δ^{199}Hg source values and uncertainties. End-member values are: volcanically emitted Hg Δ^{199}Hg = 0.02 ± 0.06‰ (Yin et al., 2016b) and terrestrial Hg Δ^{199}Hg = –0.6 ± 0.04‰ (Yin et al., 2016b, and also constrained by the mean of the 5 lowest Δ^{199}Hg values in the terrestrial Blue Anchor Formation, Fig. 2). This terrestrial value is also assumed to represent the Δ^{199}Hg of thermogenically released Hg via contact metamorphism of organic-rich sediment in **a**. However, the gradient shading in **a** indicates uncertainty in this thermogenic Δ^{199}Hg end-member value. Gray areas in **a, b** and **c** indicate possible Hg mass ranges based on reservoir size uncertainties. See main text for details.

during the ETME (Figs. 2; 3c and 3d) suggests that atmospheric photoreaction-induced Δ^{199}Hg transition was likely to have been limited. If the Hg masses involved in driving shifts B and C at St. Audrie's Bay really were low, then this may account for the lack of clear Hg enrichment in our studied rocks.

A further caveat is that the mass balance calculations assume terrestrial Hg fluxes remained constant across shifts B and C. As discusssed above, this is supported by the lack of correlation between our organic geochemical indicators of organic matter source and Δ^{199}Hg (Figs. 2 and 3b). Nevertheless, mean Δ^{199}Hg across the ETME is negative and shifts B and C occur in predominantly clay-bound Hg deposited in a near-shore environment (Fig. 2; Table. S1; Fig. S2). Thus, terrestrial Hg certainly contributed to the background Δ^{199}Hg. Terrestrial ecosystem collapse during the end-Triassic is observed around the globe (van de Schootbrugge et al., 2009; Williford et al., 2014; Fox et al., 2022b) and was likely associated with wildfire, volcanism-driven acid rain and enhanced soil erosion. Recent work has shown how increased terrestrial flux of decaying biomass immediately following ecosystem collapse could coincide with a shift in Δ^{199}Hg to lower values (Dal Corso et al., 2020; Jin et al., 2022). Subsequent to this collapse, reduced terrestrial biomass could ultimately lead to a positive Δ^{199}Hg shift. Thus, this scenario could potentially explain both shifts B and C. However, mass balance calculations suggest that a ~5.07 Mg decrease in terrestrial Hg flux would be required to drive the observed +0.48‰ Δ^{199}Hg increase at Shift C (assuming a terrestrial end-member Δ^{199}Hg of –0.6‰ ± 0.04‰; Fig. 5c). This value is nearly equal to our estimated Hg reservoir mass for the Bristol Channel Basin (5.6 Mg), and such a significant drop in terrestrial input is not evident in our organic geochemistry data, or in palynology data previously obtained through the St. Audrie's Bay succession (Bonis et al., 2010, Fig. S4). Overall, we cannot rule out that the Δ^{199}Hg signal across the ETME at St. Audrie's Bay was at least partly influenced by localized changes in terrestrial Hg flux.

Other possible influences on the Δ^{199}Hg signal across the ETME exist. For instance, the development of photic zone euxinia (PZE) can drive negative shifts in Hg odd-MIF (Zheng et al., 2018). Episodic PZE conditions from the top Westbury Formation upwards into the Blue Lias Formation are recorded by sulfur bacteria biomarker indices, which is also consistent with Fe speciation evidence for euxinia (Fox et al., 2020, 2022; He et al., 2022; Fig. S4). Nevertheless, limited data means that a clear association between redox changes and Shift B cannot be made (Fig. S4). Although the impact of PZE conditions on the Δ^{199}Hg signal is hard to quantitively evaluate, its magnitude at St. Audrie's Bay was likely to have been limited due to the formation of Hg(II) complexes in the water column stimulated by the large amount of chloride ligands (Yamamoto, 1996).

4.3. Re-evaluating the relative timing of magmatism in the ETME

The lowermost Marshi CIE, which likely marks the onset of the ETME (Lindström et al., 2021), has been associated with release of ^{12}C-enriched carbon, perhaps from early CAMP extrusives (Lindström et al., 2021). No previous Hg isotope records have extended to the Marshi CIE. In our work, neither increased Hg concentration nor any shift in Δ^{199}Hg occurs at the Marshi CIE (Fig. 2). The veracity of the Marshi CIE at St. Audrie's Bay cannot be established due to the lack of reliable biostratigraphic constraints. Another key feature of our Δ^{199}Hg record is that Shift C is 3.35 m below the Initial/Spelae CIE, which has also previously been linked to ^{12}C-enriched carbon release from extrusive volcanic outgassing (Hesselbo et al., 2002). The clear mismatch between the timing of Shift C and the Initial/Spelae CIE supports recent work that demonstrates that the Spelae CIE in this region was not, in fact, caused by volcanism, but was actually caused by local changes in organic matter linked to sea level change (Fox et al., 2020, see also Section 2). Although organic matter changes could have caused the Initial/Spelae CIE, these inferred changes do not appear to have impacted the Δ^{199}Hg signal due to the lack of corresponding change in Δ^{199}Hg at this level. The precise correlation between St Audrie's Bay and other available Triassic-Jurassic records remains highly uncertain, but the proposed correlation of Lindström et al. (2017, 2021) (shown in Fig. 4) suggests that Δ^{199}Hg shifts B and C are coincident with major intrusive and extrusive activity. If the Initial/Spelae CIE was real, and older (as per the correlation implied in Hesselbo et al., 2002 and discussed in Lindström et al., 2021), then the proposed pattern of intrusive followed by extrusive activity across shifts B and C may still be consistent with the available CAMP dates (Fig. S1), but the issues surrounding CIE correlations, and indeed the lack of agreement between CIEs and Δ^{199}Hg data, remain. Given the variable expression and likely local influences on $\delta^{13}C_{org}$ records (Fox et al., 2020, see also Lindström et al., 2021), it is possible that the timing and style of CAMP activity may be more reliably established with Δ^{199}Hg compared to $\delta^{13}C_{org}$.

The age of the continental ETME within the CAMP region, as derived from combined analysis of palynology and basalt geochronology in the Newark Basin, is 201.564 ± 0.015 Ma (Blackburn et al., 2013). The ETME age from the marine record within the CAMP region is constrained by ammonoids and interbedded ash bed dating in Peru (201.51 ± 0.15 Ma and 201.39 ± 0.14 Ma, with both dates within the interval between the LO of *Choristoceras* and the FO of *P. spelae*, Shoene et al., 2010; Wotzlaw et al., 2014). Thus, marine and continental extinction appear to be broadly synchronous (i.e. within the error of each other based on the available dates). These dates are broadly coincident with dates for CAMP intrusives into large amounts of evaporite deposits and organic-rich shales in the Amazonas basin, which suggest a major phase of thermogenic volatile emission at ~201.5 Ma (Blackburn et al., 2013; Davies et al., 2017; Heimdal et al., 2018; Marzoli et al., 2019), though there are few extrusive dates (Fig. 4). Outside the CAMP region, marine and terrestrial extinction events at St Audrie's Bay and terrestrial extinction in Denmark are broadly synchronous with inferred volcanogenic release at Δ^{199}Hg Shift C (following the correlation in Lindström et al., 2012, 2021), suggesting a key role for extrusive volcanism in driving local extinctions in the NW epicontinental sea area.

A similar sequence of mainly intrusive followed by mainly extrusive magmatism has also been geochronologically determined for other LIPs, such as end-Permian Siberian Traps (Burgess and Bowring, 2015) and early Toarcian Ferrar LIP (Burgess et al., 2015). Notably, a similar degassing style to that established here for the end-Triassic is inferred from modeling work on the end-Permian mass extinction by Wu et al. (2023). For this event, thermogenic greenhouse gas release was deemed to have had a slower emission rate than later volcanogenic emission, thus supporting volcanic CO_2 as the key trigger for environmental changes that occurred during the main end-Permian extinction event (Wu et al., 2023).

5. Conclusions

In this work, a negative shift followed by a positive shift in Δ^{199}Hg across the ETME in an epicontinental section near the northern flank of CAMP provides evidence of exogenic Hg inputs via thermogenic release from heating of organic-rich sedimentary rocks during an early intrusive phase, followed by atmospheric loading during a later explosive volcanic phase. This deduction is consistent with knowledge of CAMP emplacement and LIPs during other major paleoclimate change events. Simple mass balance considerations suggest low but plausible volumes of Hg (<50 Mg) could have driven the observed Δ^{199}Hg changes, despite the much larger volumes likely released during CAMP emplacement. Nevertheless, these masses are minimum estimates, and it is also clear that local factors such as terrestrial flux changes and PZE conditions have the potential to complicate the interpretation and quantification of Hg isotope perturbations. Despite these issues, our data demonstrate that Hg-isotope data have the potential to record at high-resolution different magmatism processes, providing important data alongside typically sparse ash bed and intrusion dates that can be hard to correlate with sedimentary records of biotic/environmental change.

CRediT authorship contribution statement

Xia Hua: Writing – original draft, Methodology, Investigation, Formal analysis. **Runsheng Yin:** Writing – review & editing, Methodology. **David B. Kemp:** Writing – review & editing, Supervision, Funding acquisition, Formal analysis, Conceptualization. **Chunju Huang:** Formal analysis, Funding acquisition, Supervision. **Jun Shen:** Writing – review & editing. **Xin Jin:** Writing – review & editing, Formal analysis.

Declaration of Competing Interest

The authors declare that they have no known competing financial interests or personal relationships that could have appeared to influence the work reported in this paper.

Data availability

Data will be made available on request.

Acknowledgement

This work was supported by the National Natural Science Foundation of China (Grant No. 42230208, 42272033, 41888101, 42172039). We thank Canfa Wang, Hongye Pei and Jiachen Fan for assistance with biomarker laboratory work, and Jacopo Dal Corso for helpful discussions. This work is a contribution to IGCP 739.

Supplementary materials

Supplementary material associated with this article can be found, in the online version, at doi:10.1016/j.epsl.2023.118438.

References

Amos, H.M., Jacob, D.J., Streets, D.G., Sunderland, E.M., 2013. Legacy impacts of all-time anthropogenic emissions on the global mercury cycle. Glob. Biogeochem. Cycles 27, 410–421.
Amos, H.M., Jacob, D.J., Kocman, D., Horowitz, H.M., Zhang, Y., Dutkiewicz, S., Horvat, M., Corbitt, E.S., Sunderland, E.M., 2014. Global biogeochemical implications of mercury discharges from rivers and sediment burial. Environ. Sci. Technol. 48, 9514–9522.
Bergquist, B.A., Blum, J.D., 2007. Mass-dependent and-independent fractionation of Hg isotopes by photoreduction in aquatic systems. Science 318 (5849), 417–420.
Berndt, C., Planke, S., Alvarez Zarikian, C.A., Frieling, J., Jones, M.T., Milett, J.M., Brinkhuis, H., Bünz, S., Svensen, H.H., Longman, J., Scherer, R.P., Karstens, J., Manton, B., Nelissen, M., Reed, B., Inge Faleide, J., Huismans, R.S., Agarwal, A., Andrews, G.D.M., Betlem, P., Bhattacharya, J., Chatterjee, S., Christopoulou, M., Clementi, V.J., Ferré, E.C., Filina, I.Y., Guo, P., Harper, D.T., Lambart, S., Mohn, G., Nakaoka, R., Tegner, C., Varela, N., Wang, M., Xu, W., Yager, S.L., 2023. Shallow-water hydrothermal venting linked to the palaeocene–eocene thermal maximum. Nat. Geosci. 16, 803–809.
Burgess, S.D., Bowring, S.A., 2015. High-precision geochronology confirms voluminous magmatism before, during, and after earth's most severe extinction. Sci. Adv. 1, e1500470.
Burgess, S.D., Bowring, S.A., Fleming, T.H., Elliot, D.H., 2015. High-precision geochronology links the Ferrar large igneous province with early-Jurassic ocean anoxia and biotic crisis. Ear. Planet. Sci. Lett. 415, 90–99.
Burgess, S.D., Muirhead, J.D., Bowring, S.A., 2017. Initial pulse of siberian traps sills as the trigger of the end-permian mass extinction. Nat. Commun. 8, 1–4.
Blackburn, T.J., Olsen, P.E., Bowring, S.A., McLean, N.M., Kent, D.V., Puffer, J., McHone, G., Rasbury, E.T., Et-Touhami, M., 2013. Zircon U-Pb geochronology links the end-Triassic extinction with the central atlantic magmatic province. Science 340 (6135), 941–945.
Blum, J.D., Sherman, L.S., Johnson, M.W., 2014. Mercury isotopes in earth and environmental sciences. Annu. Rev. Earth Planet. Sci. 42, 249–269.
Bonis, N.R., Ruhl, M., Kürschner, W.M., 2010. Milankovitch-scale palynological turnover across the Triassic–Jurassic transition at St. Audrie's Bay, SW UK. J. Geol. Soc. 167 (5), 877–888.
Bray, E.E., Evans, E.D., 1961. Distribution of n-paraffins as a clue to recognition of source beds. Geochim. Cosmochim. Acta 22 (1), 2–15.
Capriolo, M., Marzoli, A., Aradi, L.E., Ackerson, M.R., Bartoli, O., Callegaro, S., Dal Corso, J., Ernesto, M., Gouvêa Vasconcellos, E.M., De Min, A., Newton, R.J., Szabó, C., 2021. Massive methane fluxing from magma–sediment interaction in the end-triassic central atlantic magmatic Province. Nat. Commun. 12, 5534.
Charbonnier, G., Adatte, T., Föllmi, K.B., Suan, G., 2020. Effect of intense weathering and postdepositional degradation of organic matter on Hg/TOC proxy in organic-rich sediments and its implications for deep-time investigations. Geochem. Geophys. Geosyst. 21.
Dal Corso, J., Mills, B.J., Chu, D., Newton, R.J., Mather, T.A., Shu, W., Wu, Y., Tong, J., Wignall, P.B., 2020. Permo–Triassic boundary carbon and mercury cycling linked to terrestrial ecosystem collapse. Nat. Commun. 11, 2962.
Davies, J., Marzoli, A., Bertrand, H., Youbi, N., Ernesto, M., Schaltegger, U., 2017. End-Triassic mass extinction started by intrusive CAMP activity. Nat. Commun. 8, 15596.
Fendley, I.M., Mittal, T., Sprain, C.J., Marvin-DiPasquale, M., Tobin, T.S., Renne, P.R., 2019. Constraints on the volume and rate of Deccan Traps flood basalt eruptions using a combination of high-resolution terrestrial mercury records and geochemical box models. Earth Planet. Sci. Lett. 524, 115721.
Fox, C., Cui, X., Whiteside, J.H., Olsen, P.E., Summons, R.E., Grice, K., 2020. Molecular and isotopic evidence reveals the end-Triassic carbon isotope excursion is not from massive exogenous light carbon. Proc. Natl. Acad. Sci. 117 (48), 30171–30178.
Fox, C.P., Whiteside, J.H., Olsen, P.E., Cui, X., Summons, R.E., Idiz, E., Grice, K., 2022a. Two-pronged kill mechanism at the end-Triassic mass extinction. Geology 50 (4), 448–453.
Fox, C.P., Whiteside, J.H., Olsen, P.E., Grice, K., 2022b. Flame out! End-Triassic mass extinction polycyclic aromatic hydrocarbons reflect more than just fire. Earth Planet. Sci. Lett. 584, 117418.
Grasby, S.E., Them II, T.R., Chen, Z., Yin, R., Ardakani, O.H., 2019. Mercury as a proxy for volcanic emissions in the geologic record. Earth Sci. Rev. 196, 102880.
Grasby, S.E., Liu, X., Yin, R., Ernst, R.E., Chen, Z., 2020. Toxic mercury pulses into late Permian terrestrial and marine environments. Geology 48 (8), 830–833.
Gratz, L.E., Keeler, G.J., Blum, J.D., Sherman, L.S., 2010. Isotopic composition and fractionation of mercury in Great Lakes precipitation and ambient air. Environ. Sci. Technol. 44 (20), 7764–7770.
Guex, J., Bartolini, A., Atudorei, V., Taylor, D., 2004. High-resolution ammonite and carbon isotope stratigraphy across the Triassic-Jurassic boundary at New York Canyon (Nevada). Earth Planet. Sci. Lett. 225, 29–41.
He, T., Wignall, P.B., Newton, R.J., Atkinson, J.W., Keeling, J.F., Xiong, Y., Poulton, S. W., 2022. Extensive marine anoxia in the European epicontinental sea during the end-Triassic mass extinction. Glob. Planet. Change 210, 103771.
Hammer, Ø., Jones, M.J., Schneebeli-Hermann, E., Hansen, B.B., Bucher, H., 2019. Are early triassic extinction events associated with mercury anomalies? A reassessment of the Smithian/Spathian boundary extinction. Earth Sci. Rev. 195, 179–190.
Heimdal, T.H., Svensen, H.H., Ramezani, J., Iyer, K., Pereira, E., Rodrigues, R., Jones, M. T., Callegaro, S., 2018. Large-scale sill emplacement in Brazil as a trigger for the end-Triassic crisis. Sci. Rep. 8, 141.
Hesselbo, S.P., Robinson, S.A., Surlyk, F., Piasecki, S., 2002. Terrestrial and marine extinction at the Triassic-Jurassic boundary synchronized with major carbon-cycle perturbation: a link to initiation of massive volcanism? Geology 30 (3), 251–254.
Hesselbo, S.P., Robinson, S.A., Surlyk, F., 2004. Sea-level changes and facies development across potential Triassic-Jurassic boundary horizons, SW Britain. J. Geol. Soc. Lond. 161, 365–379.
Hillebrandt, A.v., Krystyn, L., Kurschner, W.M., Bonis, N.R., Ruhl, M., Richoz, S., Schobben, M.A.N., Urlichs, M., Bown, P.R., Kment, K., McRoberts, C.A., Simms, M., Tomasovych, A., 2013. The global stratotype sections and point (GSSP) for the base of the jurassic system at kuhjoch (karwendel mountains, northern calcareous alps, tyrol, Austria). Episodes 36, 162–198.
Huang, Q., Liu, Y., Chen, J., Feng, X., Huang, W., Yuan, S., Cai, H., Fu, X., 2015. An improved dual-stage protocol to pre-concentrate mercury from airborne particles for precise isotopic measurement. J. Anal. At. Spectrom. 30 (4), 957–966.
Jin, X., Zhang, F., Baranyi, V., Kemp, D.B., Feng, X., Grasby, S.E., Sun, G., Shi, Z., Chen, W., Dal Corso, J., 2022. Early Jurassic massive release of terrestrial mercury linked to floral crisis. Earth Planet. Sci. Lett. 598, 117842.
Jin, X., Tomimatsu, Y., Yin, R., Onoue, T., Franceschi, M., Grasby, S.E., Du, Y., Rigo, M., 2023. Climax in Wrangellia LIP activity coincident with major Middle Carnian (Late Triassic) climate and biotic changes: mercury isotope evidence from the Panthalassa pelagic domain. Earth Planet. Sci. Lett 607, 118075.
Lindström, S., van de Schootbrugge, B., Dybkjaer, K., Pedersen, G.K., Fiebig, J., Nielsen, L.H., Richoz, S., 2012. No causal link between terrestrial ecosystem change and methane release during the end-Triassic mass extinction. Geology 40, 531–534.
Lindström, S., van de Schootbrugge, B., Hansen, K.H., Pedersen, G.K., Alsen, P., Thibault, N., Dybkjær, K., Bjerrum, C.J., Nielsen, L.H., 2017. A new correlation of Triassic-Jurassic boundary successions in NW Europe, Nevada and Peru, and the Central Atlantic Magmatic Province: a time-line for the end-Triassic mass extinction. Palaeogeogr. Palaeoclimatol. Palaeoecol. 478, 80–102.
Lindström, S., Sanei, H., van de Schootbrugge, B., Pedersen, G.K., Lesher, C.E., Tegner, C., Heunisch, C., Dybkjær, K., Outridge, P.M., 2019. Volcanic mercury and mutagenesis in land plants during the end–Triassic mass extinction. Sci. Adv. 5, eaaw4018.
Lindström, S., Callegaro, S., Davies, J., Tegner, C., van De Schootbrugge, B., Pedersen, G. K., Youbi, N., Sanei, H., Marzoli, A., 2021. Tracing volcanic emissions from the Central Atlantic Magmatic Province in the sedimentary record. Earth Sci. Rev. 212, 103444.
Macquaker, J.H.S., 1987. The Depositional and Diagenetic History of the Westbury Formation (Upper Triassic) in South West Britain (Doctoral dissertation. University of Bristol.
Marzoli, A., Callegaro, S., Dal Corso, J., Davies, J.H.F.L., Chiaradia, M., Youbi, N., Bertrand, H., Reisberg, L., Merle, R., Jourdan, F., 2018. The Central Atlantic Magmatic Province (CAMP): A review, The Late Triassic World. Springer, Cham.

Marzoli, A., Bertrand, H., Youbi, N., Callegaro, S., Merle, R., Reisberg, L., Chiaradia, M., Brownlee, S., Jourdan, F., Zanetti, A., Davies, J.H.F.L., Cuppone, T., Mahmoudi, A., Medina, F., Renne, P.R., Bellieni, G., Crivellari, S., El Hachimi, H., Bensalah, M.K., Meyzen, C.M., Tegner, C., 2019. The central atlantic magmatic province (CAMP) in Morocco. J. Petrol. 60, 945–996.

McElwain, J.C., Beerling, D.J., Woodward, F.I., 1999. Fossil plants and global warming at the Triassic–Jurassic boundary. Science 285, 1386–1390.

McInerney, F.A., Wing, S.L., 2011. The paleocene-eocene thermal maximum: a perturbation of carbon cycle, climate, and biosphere with implications for the future. Annu. Rev. Earth Planet. Sci. 39, 489–516.

McHone, 2003. Volatile emissions from central atlantic magmatic province basalts: mass assumptions and environmental consequences. In: The Central Atlantic Magmatic Province: Insights from Fragments of Pangea, 136. AGU Geophysical Monograph, pp. 241–254.

Park, J., Stein, H.J., Georgiev, S.V., Hannah, J.L., 2022. Degradation of Hg signals on incipient weathering: core versus outcrop geochemistry of Upper Permian shales, East greenland and mid-norwegian shelf. Chem. Geol. 608, 121030.

Percival, L.M.E., Ruhl, M., Hesselbo, S.P., Jenkyns, H.C., Mather, T.A., Whiteside, J.H., 2017. Mercury evidence for pulsed volcanism during the end-Triassic mass extinction. Proc. Natl. Acad. Sci. 114, 7929–7934.

Peters, K.E., Walters, C.C., Moldowan, J.M., 2005. The Biomarker Guide, 1. Cambridge University Press.

Poynter, J.G., Eglinton, G., et al., 1990. Molecular composition of three sediments from hole 717C: the Bengal Fan. In: Proceedings of the Ocean Drilling Program Scientific Results, 116, pp. 155–161.

Ruhl, M., Kürschner, W.M., Krystyn, L., 2009. Triassic–Jurassic organic carbon isotope stratigraphy of key sections in the western Tethys realm (Austria). Earth Planet. Sci. Lett. 281, 169–187.

Ruhl, M., Hesselbo, S.P., Al-Suwaidi, A., Jenkyns, H.C., Damborenea, S.E., Manceñido, M.O., Storm, M., Riccardi, A.C., 2020. On the onset of central atlantic magmatic province (CAMP) volcanism and environmental and carbon-cycle change at the Triassic–Jurassic transition (Neuquén Basin, Argentina). Earth Sci. Rev. 208, 103229.

Schoene, B., Guex, J., Bartolini, A., Schaltegger, U., Blackburn, T.J., 2010. Correlating the end-Triassic mass extinction and flood basalt volcanism at the 100 ka level. Geology 38, 387–390.

Scotese, C.R., 2014. Atlas of Middle & Late Permian and Triassic Paleogeographic Maps, Maps 43 - 48 from Volume 3 of the PALEOMAP Atlas for ArcGIS (Jurassic and Triassic) and Maps 49 –52 from Volume 4 of the PALEOMAP PaleoAtlas for ArcGIS (Late Paleozoic), Mollweide Projection. PALEOMAP Project, Evanston, IL.

Selin, N.E., 2009. Global biogeochemical cycling of mercury: a review. Annu. Rev. Environ. Resour. 34, 43–63.

Shen, J., Feng, Q., Algeo, T.J., Liu, J., Zhou, C., Wei, W., Liu, J., Them II, T.R., Gill, B.C., Chen, J., 2020. Sedimentary host phases of mercury (Hg) and implications for use of Hg as a volcanic proxy. Earth Planet. Sci. Lett. 543, 116333.

Shen, J., Yin, R., Algeo, T.J., Svensen, H.H., Schoepfer, S.D., 2022a. Mercury evidence for combustion of organic-rich sediments during the end–Triassic crisis. Nat. Commun. 13, 1307.

Shen, J., Yin, R., Zhang, S., Algeo, T.J., Bottjer, D.J., Yu, J., Xu, G., Penman, D., Wang, Y., Li, L., Shi, X., Planavsky, N.J., Feng, Q., Xie, S., 2022b. Intensified continental chemical weathering and carbon-cycle perturbations linked to volcanism during the Triassic–Jurassic transition. Nat. Commun. 13, 299.

Shen, J., Chen, J., Yu, J., Algeo, T.J., Smith, R.M., Botha, J., Frank, T.D., Fielding, C.R., Ward, P.D., Mather, T.A., 2023. Mercury evidence from southern Pangea terrestrial sections for end-Permian global volcanic effects. Nat. Commun. 14, 6.

Svensen, H.H., Jones, M.J., Percival, L.M.E., Grasby, S.E., Mather, T.A., 2023. Release of mercury during contact metamorphism of shale: implications for understanding the impacts of large igneous province volcanism. Earth Planet. Sci. Lett. 619, 118306.

Thibodeau, A.M., Ritterbush, K., Yager, J.A., West, A.J., Ibarra, Y., Bottjer, D.J., Berelson, W.M., Bergquist, B.A., Corsetti, F.A., 2016. Mercury anomalies and the timing of biotic recovery following the end-Triassic mass extinction. Nat. Commun. 7, 11147.

van de Schootbrugge, B., Quan, T.M., Lindström, S., Püttmann, W., Heunisch, C., Pross, J., Fiebig, J., Petschick, R., Röhling, H.G., Richoz, S., Rosenthal, Y., Falkowski, P.G., 2009. Floral changes across the Triassic/Jurassic boundary linked to flood basalt volcanism. Nat. Geosci. 2, 589–594.

Warrington, G., Whittaker, A., 1984. The blue anchor formation (late Triassic) in somerset. Proc. Ussher Soc. 6, 100–107.

Williford, K.H., Grice, K., Holman, A., McElwain, J.C., 2014. An organic record of terrestrial ecosystem collapse and recovery at the Triassic–Jurassic boundary in East Greenland. Geochim. Cosmochim. Acta 127, 251–263.

Wotzlaw, J.F., Guex, J., Bartolini, A., Gallet, Y., Krystyn, L., McRoberts, C.A., Taylor, D., Schoene, B., Schaltegger, U., 2014. Towards accurate numerical calibration of the Late Triassic: high-precision U-Pb geochronology constraints on the duration of the Rhaetian. Geology 42, 571–574.

Wu, Y., Cui, Y., Chu, D., Song, H., Tong, J., Dal Corso, J., Ridgwell, A., 2023. Volcanic CO2 degassing postdates thermogenic carbon emission during the end-Permian mass extinction. Sci. Adv. 9 (7), eabq4082.

Yager, J.A., West, A.J., Corsetti, F.A., Berelson, W.M., Rollins, N.E., Rosas, S., Bottjer, D. J., 2017. Duration of and decoupling between carbon isotope excursions during the end-Triassic mass extinction and central atlantic magmatic province emplacement. Earth Planet. Sci. Lett. 473, 227–236.

Yager, J.A., West, A.J., Thibodeau, A.M., Corsetti, F.A., Rigo, M., Berelson, W.M., Bottjer, D.J., Greene, S.E., Ibarra, Y., Jadoul, F., Ritterbush, K.A., Rollins, N., Rosas, S., Di Stefano, P., Sulca, D., Todaro, S., Wynn, P., Zimmermann, L., Bergquist, B.A., 2021. Mercury contents and isotope ratios from diverse depositional environments across the Triassic–Jurassic Boundary: towards a more robust mercury proxy for large igneous province magmatism. Earth Sci. Rev. 223, 103775.

Yamamoto, M., 1996. Stimulation of elemental mercury oxidation in the presence of chloride ion in aquatic environments. Chemosphere 32 (6), 1217–1224.

Yin, R., Chen, D., Pan, X., Deng, C., Chen, L., Song, X., Yu, S., Zhu, C., Wei, X., Xu, Y., Feng, X., Blum, J.D., Lehmann, B., 2022. Mantle Hg isotopic heterogeneity and evidence of oceanic Hg recycling into the mantle. Nat. Commun. 13, 948.

Yin, R., Krabbenhoft, D.P., Bergquist, B.A., Zheng, W., Lepak, R.F., Hurley, J.P., 2016a. Effects of mercury and thallium concentrations on high precision determination of mercury isotopic composition by Neptune Plus multiple collector inductively coupled plasma mass spectrometry. J. Anal. At. Spectrom. 31 (10), 2060–2068.

Yin, R.S., Feng, X., Hurley, J.P., Krabbenhoft, D.P., Lepak, R.F., Hu, R., Zhang, Q., Li, Z., Bi, X., 2016b. Mercury isotopes as proxies to identify sources and environmental impacts of mercury in sphalerites. Sci. Rep. 6, 18686.

Zerkle, A.L., Yin, R., Chen, C., Li, X., Izon, G.J., Grasby, S.E., 2020. Anomalous fractionation of mercury isotopes in the Late Archean atmosphere. Nat. commun. 11 (1), 1709.

Zhang, Y., Jaeglé, L., Thompson, L., 2014. Natural biogeochemical cycle of mercury in a global three- dimensional ocean tracer model. Glob. Biogeochem. Cycle 28, 553–570.

Zheng, W., Gilleaudeau, G.J., Kah, L.C., Anbar, A.D., 2018. Mercury isotope signatures record photic zone euxinia in the Mesoproterozoic ocean. Proc. Natl. Acad. Sci. 115 (42), 10594–10599.